

# Temperature and density fluctuations in the inner Orion Nebula

W. J. Henney, C. R. O'Dell, G. J. Ferland, M. Peimbert

## 1. Analysis

### 1.1. Deriving diagnostic line ratios from WFC3 filter images

*Note: this is similar to what I wrote in the calibration draft, but specifically tailored to line ratios rather than equivalent widths. We may in the end want to move some of it back to the other paper.*

The WFC3 camera is equipped with filters that effectively target important nebular diagnostic lines. Each filter, with label  $j$ , is characterized by an effective transmission profile, or throughput,  $T_\lambda^j$ , which gives the wavelength-dependent conversion factor between the number of photons arriving at the *HST* entrance aperture (nominal radius: 120 cm) and the number of electrons registered by the CCD, accounting for occultation by the secondary mirror, all other optical and quantum efficiencies, and the amplifier gain. The peak value of the filter transmission profile is denoted  $T_m^j$ , with typical values of 0.2–0.3, and the “rectangular width” of the profile is defined as

$$W_j = (T_m^j)^{-1} \int_0^\infty T_\lambda^j d\lambda \quad [W_j] = \text{\AA}. \quad (1)$$

Extensive and continuing on-orbit calibration of the filters has been carried out (Kalirai et al. 2009, 2010; Sabbi & the WFC3 Team 2013) using white dwarf standard stars. However, since these are flat featureless continuum sources, the calibration is only sensitive to the integrated filter throughput, given by the product  $W_j T_m^j$ . A general increase in the integrated throughput of 10–20% with respect to pre-launch measurements was found for all filters, which was fitted by a low-order polynomial as a function of frequency. Only the broad-band and medium-band filters were used in determining the fit, but the scatter of the narrow-band filters<sup>1</sup> around the resulting curve is only a few percent (see Fig. 6 of Kalirai et al. 2009).

Emission lines from photoionized regions are intrinsically much narrower than even the narrowest WFC3 filters, so the transmission of such a line, with label  $i$ , is independent of  $W_j$  and depends instead solely on the throughput at the line wavelength:  $T_i^j \equiv T_\lambda^j(\lambda = \lambda_i)$ . The detailed shape of the throughput curves was measured pre-launch (Brown 2006), but direct on-orbit confirmation of these curves is impossible. However, by comparing WFC3 images with ground-based spectrophotometry of emission line nebulae, it is possible to test the filter calibrations for the case where emission lines are the dominant component of the spectrum in the filter bandpass. Just such a calibration is described in detail in a companion paper (Henney et al. 2014), using multiple spectrophotometric datasets of the Orion Nebula (M42) and the evolved nearby planetary nebula NGC 6720 (the Ring Nebula), and building on an earlier study in O'Dell et al. (2013). The conclusion of this study is that the nominal filter parameters (that is, the pre-launch measurements of the shape of the throughput curve  $T_\lambda^j$ , combined with the on-orbit re-calibration of  $W_j T_m^j$ ), are consistent to within  $\pm 5\%$  with the emission line spectrophotometry for all but a handful of filters. The largest discrepancy is found for the F469N filter, which is found to have a sensitivity to the He II  $\lambda 4686$  line that is 35% higher than the nominal

---

<sup>1</sup>Note, however, that the quad filters were not included in these studies.

value. However, that line is absent in M42, due to the relatively low effective temperature of the ionizing star, and the filter is instead dominated by continuum and weak [Fe III] lines. In such circumstance the nominal F469N parameters are found to be accurate.

Smaller, but still significant, discrepancies are found for the F658N and FQ575N filters, which target the [N II] lines  $\lambda 6583$  and  $\lambda 5755$ , respectively. *Discuss inconsistency between Ring and Orion calibration. Ring has 5755 increased by 10%. Orion has 6583 decreased by 10%. But effects on ratio are similar.*

We model the specific intensity,  $I_\lambda$  (in  $\text{erg s}^{-1} \text{cm}^{-2} \text{sr}^{-1} \text{\AA}^{-1}$ ), of a spatially resolved astrophysical source as the sum of several narrow emission lines  $i$ , each with central wavelength  $\lambda_i$  and wavelength-integrated intensity  $I_i$ , plus a slowly varying continuum  $I_\lambda^c$ :

$$I_\lambda = I_\lambda^c + \sum_{i=1,n} I_i \delta(\lambda - \lambda_i), \quad (2)$$

where  $\delta$  denotes the Dirac delta function. It is convenient to define an average continuum intensity over the passband of filter  $j$ :

$$\langle \lambda I_\lambda^c \rangle_j = \int_0^\infty \lambda I_\lambda^c T_\lambda^j d\lambda / \int_0^\infty T_\lambda^j d\lambda. \quad (3)$$

The count rate (in  $\text{e}^-/\text{s}$ ) in a single pixel of a pipeline-reduced (bias-subtracted, flat-fielded, drizzled) WFC3 image should then be

$$R_j = C_{\text{WFC3}} \left( \langle \lambda I_\lambda^c \rangle_j T_m^j W_j + \sum_{i=1,n} \lambda_i I_i T_i^j \right) \quad (4)$$

where  $C_{\text{WFC3}} = 10^{-8} A_{\text{HST}} \Omega_{\text{pix}} / (hc) = 0.0840241 \text{ counts cm}^2 \text{sr erg}^{-1} \text{\AA}^{-1} \text{pixel}^{-1}$  is a constant for the camera, depending on the telescope aperture area,  $A_{\text{HST}} = \pi(120 \text{ cm})^2 = 45,239 \text{ cm}^2$ , and the solid-angle subtended<sup>2</sup> by each pixel  $\Omega_{\text{pix}} = (0.03962'')^2 = 3.6895 \times 10^{-14} \text{ sr}$ .

We now consider the particular application of deriving a diagnostic ratio between two emission lines:  $I_1/I_2$ . It is assumed that observations are made in three filters: Filter I, which targets line 1, Filter II, which targets line 2, and Filter III, which targets the continuum. For optimum results, filters I and II will be narrow-band in order to admit as little continuum as possible, while III will be medium-band so as to efficiently sample the continuum, while at the same time avoiding strong emission lines. However, in practice it is usually impossible to completely avoid emission line contamination of filter III, either by one or both of the target lines (1 and 2), or by other lines that we denote  $i'$ . A schematic illustration of this situation is given

---

<sup>2</sup>Although geometric distortions by the telescope optics mean that the true pixel area varies across the field of view, this is corrected for during the “drizzle” stage of the pipeline reduction process, which yields images (extension drz) interpolated onto a regular pixel grid. If non-drizzled (extension f1t) images are used, then a further correction for the pixel area map must be applied to equation (4).

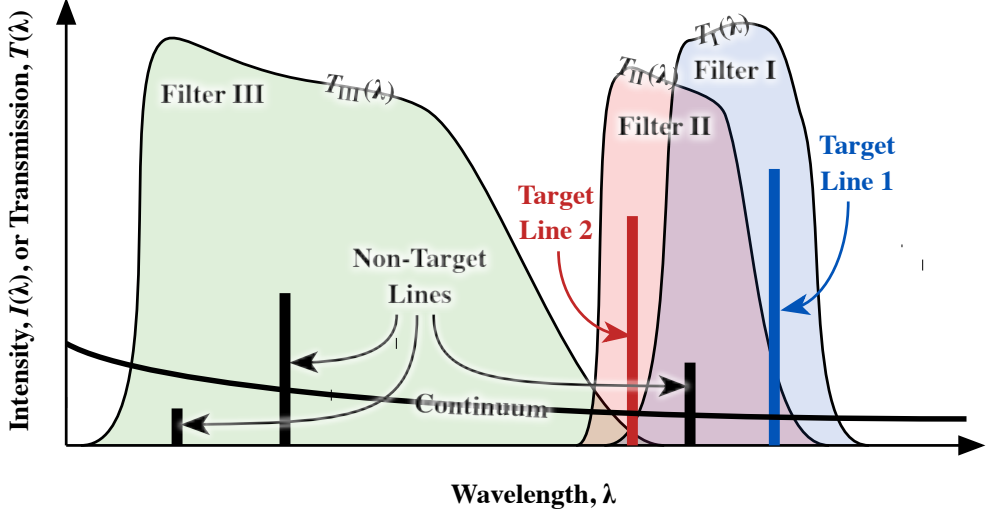


Fig. 1.— Schematic illustration of how the intensity ratio between two target lines is derived using observations in three filters.

in Figure 1. For given line and continuum intensities,  $I_1, I_2, I_\lambda^c$ , the predicted filter rates are:

$$R_{\text{I}} = C_{\text{WFC3}} \left[ \langle \lambda I_\lambda^c \rangle_{\text{I}} T_{\text{m}}^{\text{I}} W_{\text{I}} + \lambda_1 I_1 T_1^{\text{I}} + \lambda_2 I_2 T_2^{\text{I}} + \sum_{i' \neq 1,2} \lambda_{i'} I_{i'} T_{i'}^{\text{I}} \right] \quad (5)$$

$$R_{\text{II}} = C_{\text{WFC3}} \left[ \langle \lambda I_\lambda^c \rangle_{\text{II}} T_{\text{m}}^{\text{II}} W_{\text{II}} + \lambda_1 I_1 T_1^{\text{II}} + \lambda_2 I_2 T_2^{\text{II}} + \sum_{i' \neq 1,2} \lambda_{i'} I_{i'} T_{i'}^{\text{II}} \right] \quad (6)$$

$$R_{\text{III}} = C_{\text{WFC3}} \left[ \langle \lambda I_\lambda^c \rangle_{\text{III}} T_{\text{m}}^{\text{III}} W_{\text{III}} + \lambda_1 I_1 T_1^{\text{III}} + \lambda_2 I_2 T_2^{\text{III}} + \sum_{i' \neq 1,2} \lambda_{i'} I_{i'} T_{i'}^{\text{III}} \right] \quad (7)$$

The mean continuum intensity in the narrow filters can be related to that in the wider filter by defining color terms:

$$k_{j,\text{III}} \equiv \frac{\langle \lambda I_\lambda^c \rangle_j}{\langle \lambda I_\lambda^c \rangle_{\text{III}}} \quad \text{for } j = \text{I, II} \quad (8)$$

The filter color terms can be formally extended to include the contribution of contaminating non-target emission lines:

$$\tilde{k}_{j,\text{III}} \equiv \frac{\langle \lambda I_\lambda^c \rangle_j + (T_{\text{m}}^j W_j)^{-1} \sum_{i' \neq 1,2} \lambda_{i'} I_{i'} T_{i'}^j}{\langle \lambda I_\lambda^c \rangle_{\text{III}} + (T_{\text{m}}^{\text{III}} W_{\text{III}})^{-1} \sum_{i' \neq 1,2} \lambda_{i'} I_{i'} T_{i'}^{\text{III}}} = \frac{\left(1 + \sum_{i' \neq 1,2} E_{i'} / \tilde{W}_{j,i'}\right) k_{j,\text{III}}}{1 + \sum_{i' \neq 1,2} E_{i'} / \tilde{W}_{\text{III},i'}} \quad (9)$$

where the  $E_{i'}$  are the equivalent width (in Å) of each non-target line and we have also introduced an “effective width” of each filter with respect to a given emission line:

$$\tilde{W}_{j,i} \equiv k_{j,i} \frac{T_{\text{m}}^j}{T_i^j} W_j \quad \text{with} \quad k_{j,i} \equiv \frac{\langle \lambda I_\lambda^c \rangle_j}{\lambda_i I_\lambda^i}. \quad (10)$$

Note that the effective width has the property that  $\tilde{W}_{j,i} \simeq W_j$  for lines  $i$  that lie comfortably within the bandpass of filter  $j$ , whereas  $\tilde{W}_{j,i} > W_j$  for lines that lie on the edge of the bandpass, where the filter transmission is reduced, and  $\tilde{W}_{j,i} \rightarrow \infty$  for lines far-removed from the filter bandpass.

Table 1: Filter contamination coefficients, see eq. (11)

Ratio: $I_1/I_2$	Filter Set: I, II, III	$\alpha_1$	$\alpha_2$	$\beta_1$	$\beta_{\text{II}}$	$\gamma_1$	$\gamma_2$
[N II] 5755/6583	FQ575N, F658N, F547M	0.7946	~ 0	0.0243	0.0394	~ 0	~ 0
[S II] 6716/6731	FQ672N, FQ674N, F673N	1.0580	1.2510	0.1640	0.1142	0.0702	0.0056
[S II] 6716/6731	FQ672N, FQ674N, F547M	~ 0	~ 0	0.0274	0.0191	0.0702	0.0050
[O III] 4363/5007	FQ437N, F502N, FQ436N	0.9170	~ 0	0.711	1.998	~ 0	~ 0
[O III] 4363/5007	FQ437N, F502N, F547M	~ 0	0.0016	0.0343	0.0963	~ 0	~ 0
H $\beta$ /H $\alpha$ 4861/6563	F487N, F656N, F547M	~ 0	~ 0	0.0871	0.0238	~ 0	~ 0
[N II]/H $\alpha$ 6583/6563	F658N, F656N, F547M	~ 0	~ 0	0.0394	0.0238	~ 0	0.0022
[O III]/H $\beta$ 5007/4861	F502N, F487N, F547M	0.0016	~ 0	0.0963	0.0871	~ 0	~ 0

Note: Values marked as “~ 0” are all less than  $10^{-5}$ .

With these definitions, equations (5) to (7) can be recognised as being equivalent to a single matrix equation that gives the vector of count rates,  $[R_{\text{I}}; R_{\text{II}}; R_{\text{III}}]$ , in terms of the vector of intensities,  $[\lambda_1 I_1; \lambda_2 I_2; \langle \lambda I_{\lambda}^{\text{c}} \rangle_{\text{III}}]$ . Therefore, in order to solve for the intensities in terms of the count rates it is sufficient to invert the matrix. The result for the line ratio is then:

$$\frac{I_1}{I_2} = \frac{\lambda_2 T_2^{\text{II}}}{\lambda_1 T_1^{\text{I}}} \frac{[(1 - \alpha_2 \beta_{\text{II}} \tilde{k}_{\text{II,III}}) R_{\text{I}} + (\alpha_2 \beta_{\text{II}} \tilde{k}_{\text{II,III}} - \gamma_2) R_{\text{II}} + (\gamma_2 \beta_{\text{II}} \tilde{k}_{\text{II,III}} - \beta_{\text{II}} \tilde{k}_{\text{II,III}}) R_{\text{III}}]}{[(\alpha_1 \beta_{\text{II}} \tilde{k}_{\text{II,III}} - \gamma_1) R_{\text{I}} + (1 - \alpha_1 \beta_{\text{II}} \tilde{k}_{\text{II,III}}) R_{\text{II}} + (\gamma_1 \beta_{\text{II}} \tilde{k}_{\text{II,III}} - \beta_{\text{II}} \tilde{k}_{\text{II,III}}) R_{\text{III}}} \quad (11)$$

with filter contamination coefficients

$$\alpha_1 = \frac{T_1^{\text{III}}}{T_1^{\text{I}}}; \quad \alpha_2 = \frac{T_2^{\text{III}}}{T_2^{\text{II}}}; \quad \beta_{\text{I}} = \frac{T_{\text{m}}^{\text{I}} W_{\text{I}}}{T_{\text{m}}^{\text{III}} W_{\text{III}}}; \quad \beta_{\text{II}} = \frac{T_{\text{m}}^{\text{II}} W_{\text{II}}}{T_{\text{m}}^{\text{III}} W_{\text{III}}}; \quad \gamma_1 = \frac{T_1^{\text{II}}}{T_1^{\text{I}}}; \quad \gamma_2 = \frac{T_2^{\text{I}}}{T_2^{\text{II}}}.$$

The  $\alpha$  contamination coefficients give the throughput of each target emission line in the continuum filter III relative to the throughput in its respective narrow-band filter, and will tend to be either  $\sim 1$  for lines that fall in the continuum bandpass, or  $\sim 0$  for those that do not. The  $\beta$  contamination coefficients give the integrated continuum throughput in each narrow band filter relative to the continuum filter. The  $\gamma$  contamination coefficients give the throughput of each target emission line in the “other” narrow band filter relative to the throughput in its own narrow-band filter, and will only be important in cases where the two narrow band filters overlap.

Since repeated calibration programs have shown that the WFC3 filter characteristics are stable with time, all these purely instrumental coefficients are constants, albeit with a small systematic uncertainty in their true value. The  $\tilde{k}$  factors, on the other hand, represent the relative strengths of the continuum and non-target lines in the bandpasses of the three filters, and are expected to show variations from object to object and from pixel to pixel within the same object, due to changes in the physical conditions.

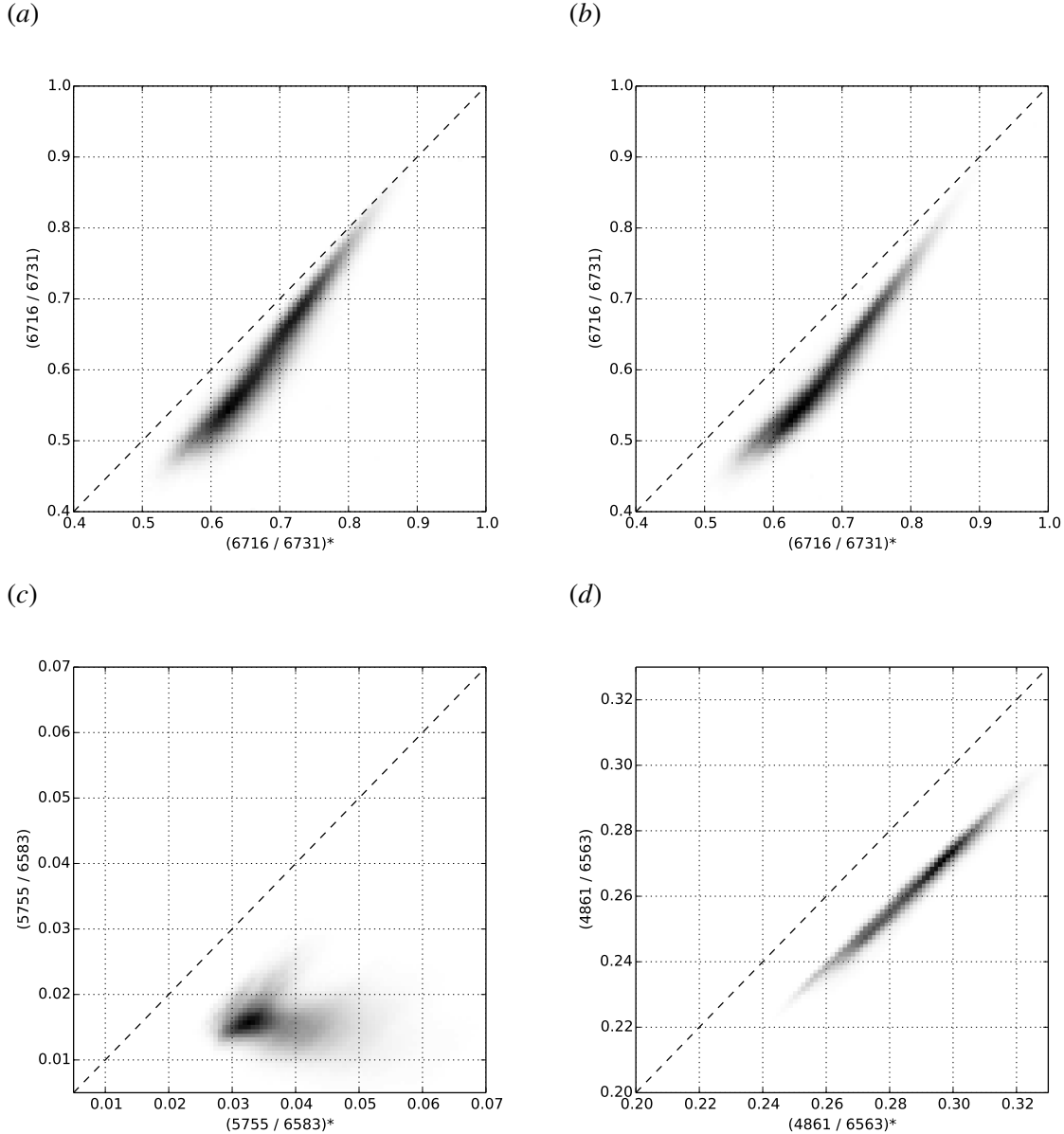


Fig. 2.— Effects on derived line ratios of contamination by continuum and non-target lines. In each panel, the  $x$  axis shows the “naive” line ratio, while the  $y$  axis shows the corrected line ratio. (a) [S II] 6716/6731 ratio calculated from FQ672N, FQ674N, F673N; (b) [S II] 6716/6731 ratio calculated from FQ672N, FQ674N, F547M; (c) [N II] 5755/6583 ratio calculated from FQ575N, F658N, F547M; (d) H $\beta$ /H $\alpha$  ratio calculated from F487N, F656N, F547M.

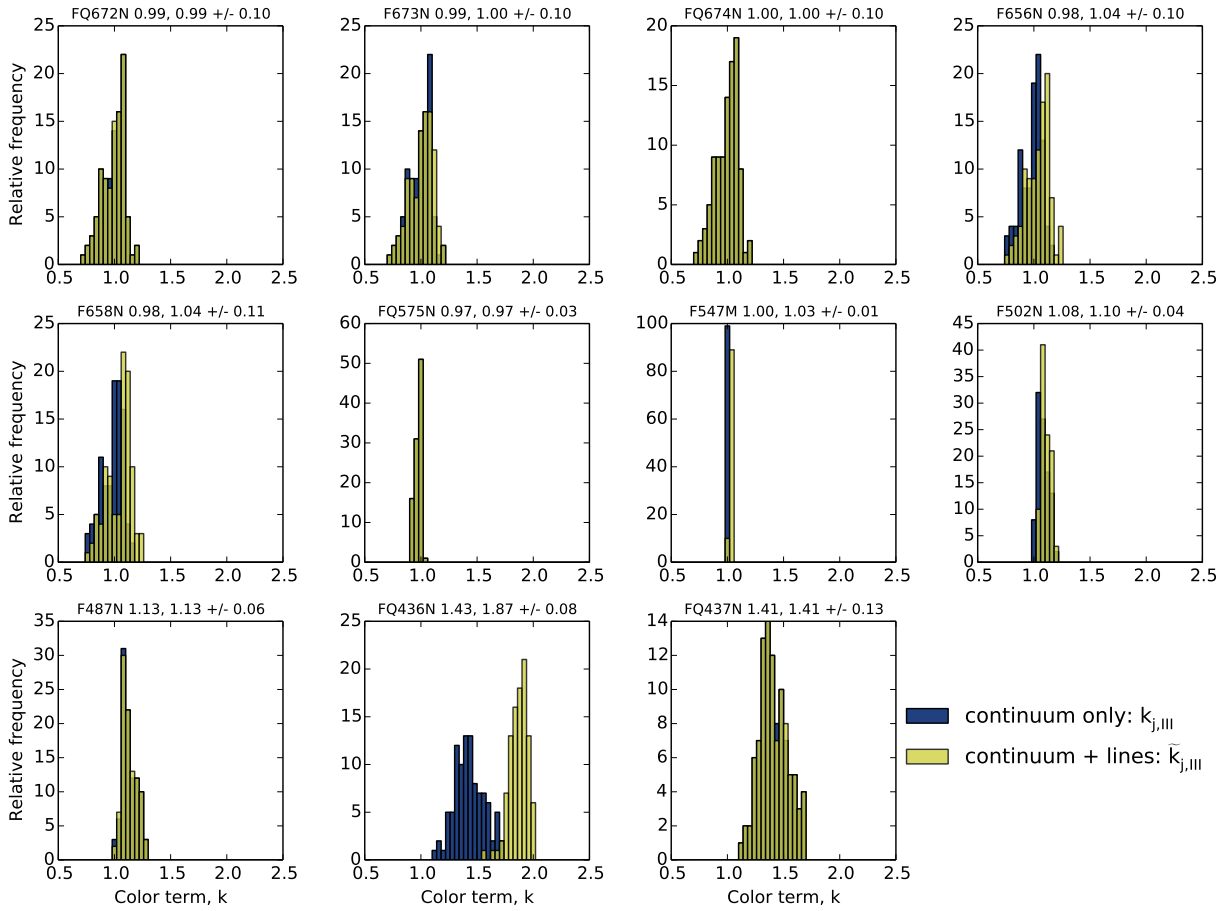


Fig. 3.— Observationally determined histograms of the color correction terms,  $k$ , for each filter with respect to the F547M filter, measured from spectrophotometry of the Orion Nebula (O’Dell & Harris 2010). The blue histograms show the ratio of the mean continuum intensity in each filter to that in F547M, as given by equation (8), while the yellow histograms include the additional effect of non-target emission lines and correspond to the numerator of fraction on the RHS of equation (9), except for F547M where they correspond to the denominator of that fraction.

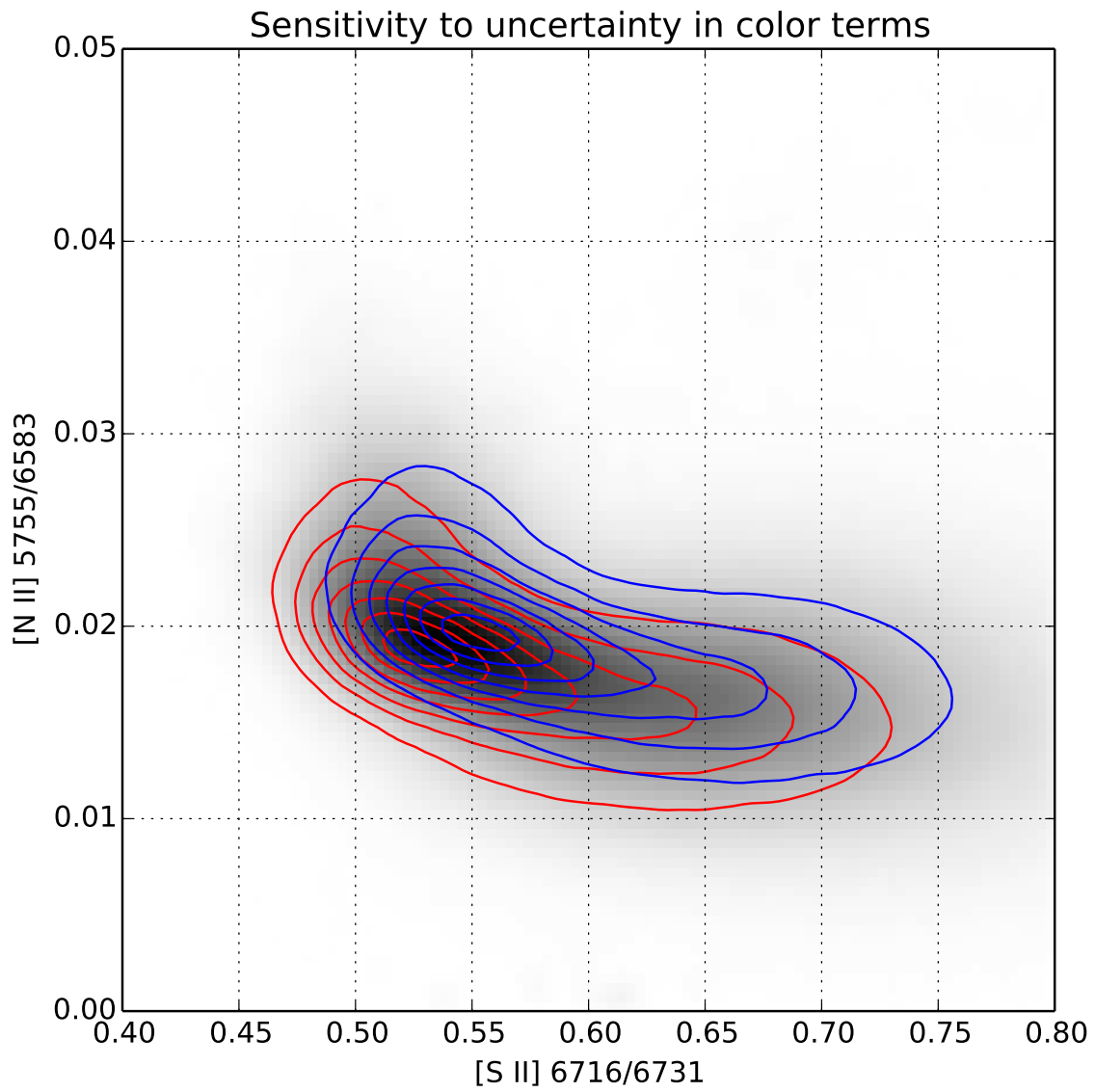


Fig. 4.— Sensitivity of the derived line ratios to spatial variations in the color correction terms.

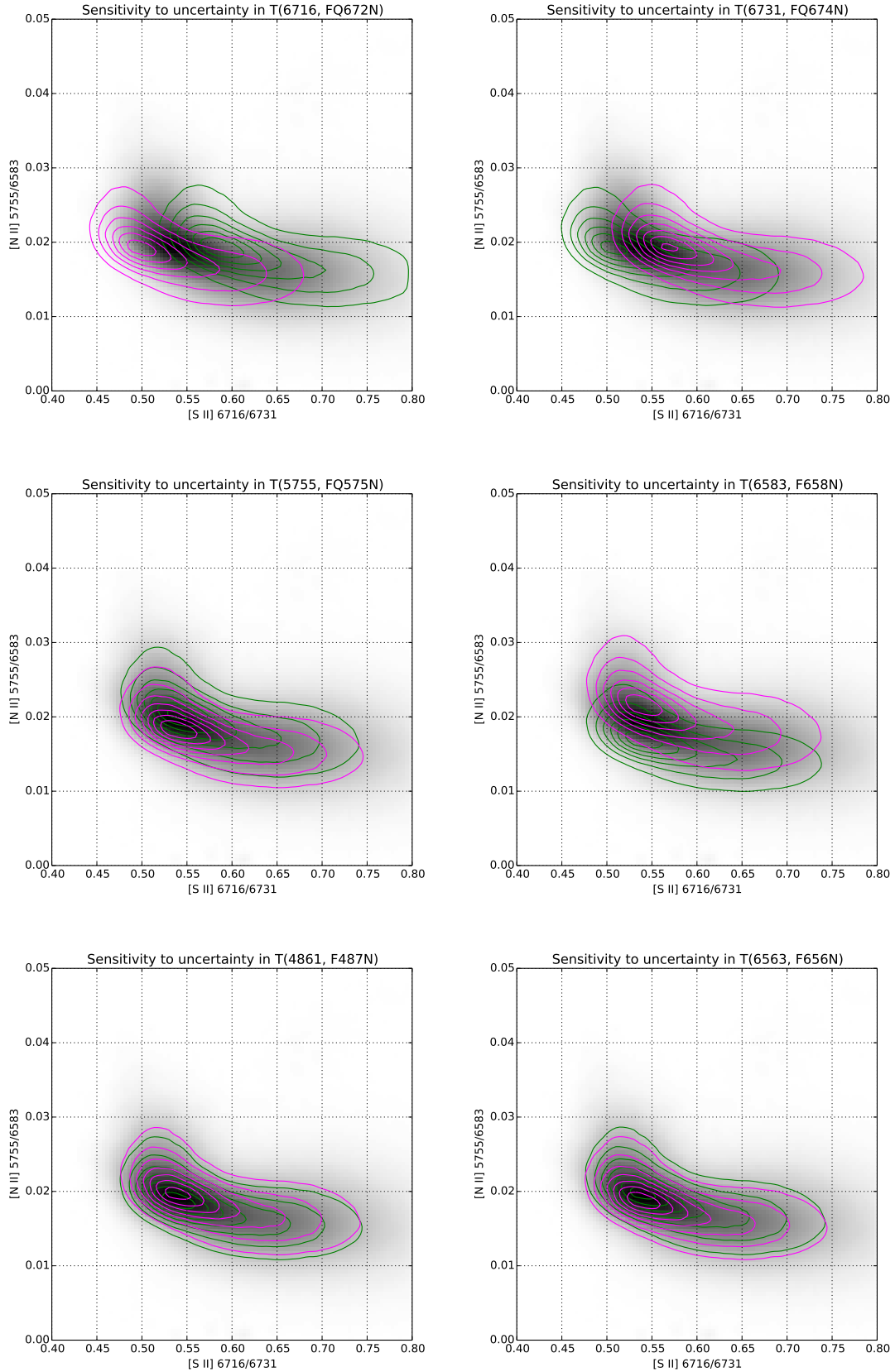


Fig. 5.— Sensitivity of the derived line ratios to systematic uncertainties in the emission line filter throughputs.

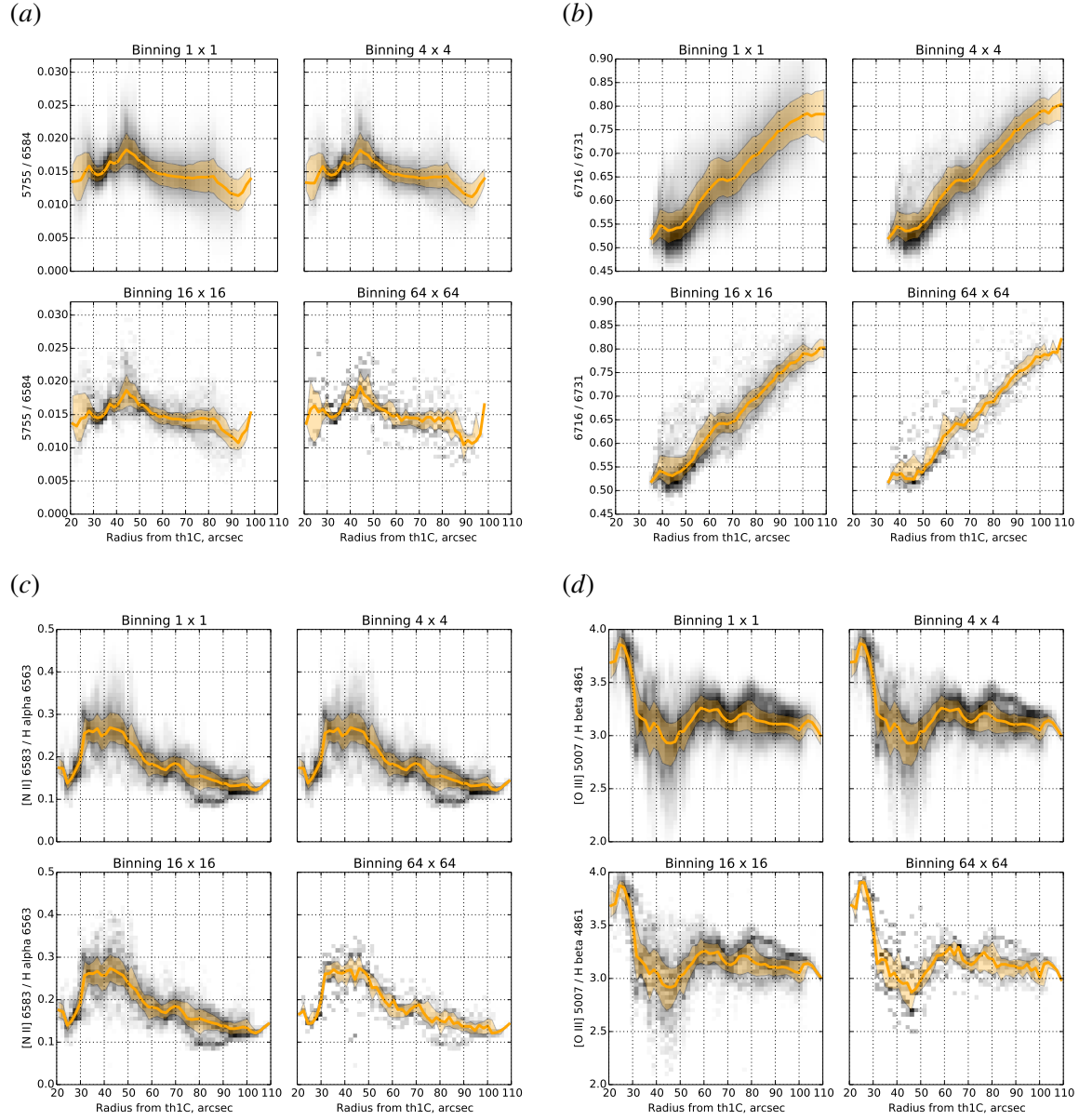


Fig. 6.— Distributions of line ratios as a function of radius. (a) [N II] 5755/6584. (b) [S II] 6716/6731. (c) [N II] 6583/H $\alpha$  6563. (d) [O III] 5007/H $\beta$  4861. In all cases the weighting is by H $\alpha$  surface brightness and four cases are shown with binnings of  $1 \times 1$ ,  $4 \times 4$ ,  $16 \times 16$ , and  $64 \times 64$  pixels.

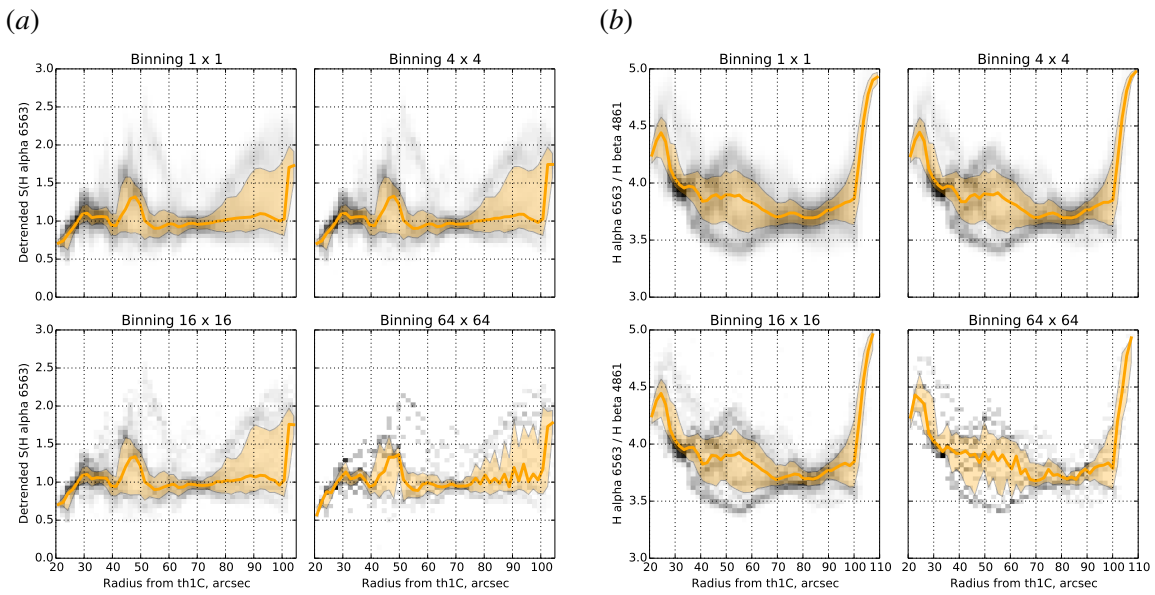


Fig. 7.— Same as Fig. 6 but for the dereddened surface brightness of the H $\alpha$  line after detrending, that is removing a large scale variation with radius of  $R^{-1.4}$ .

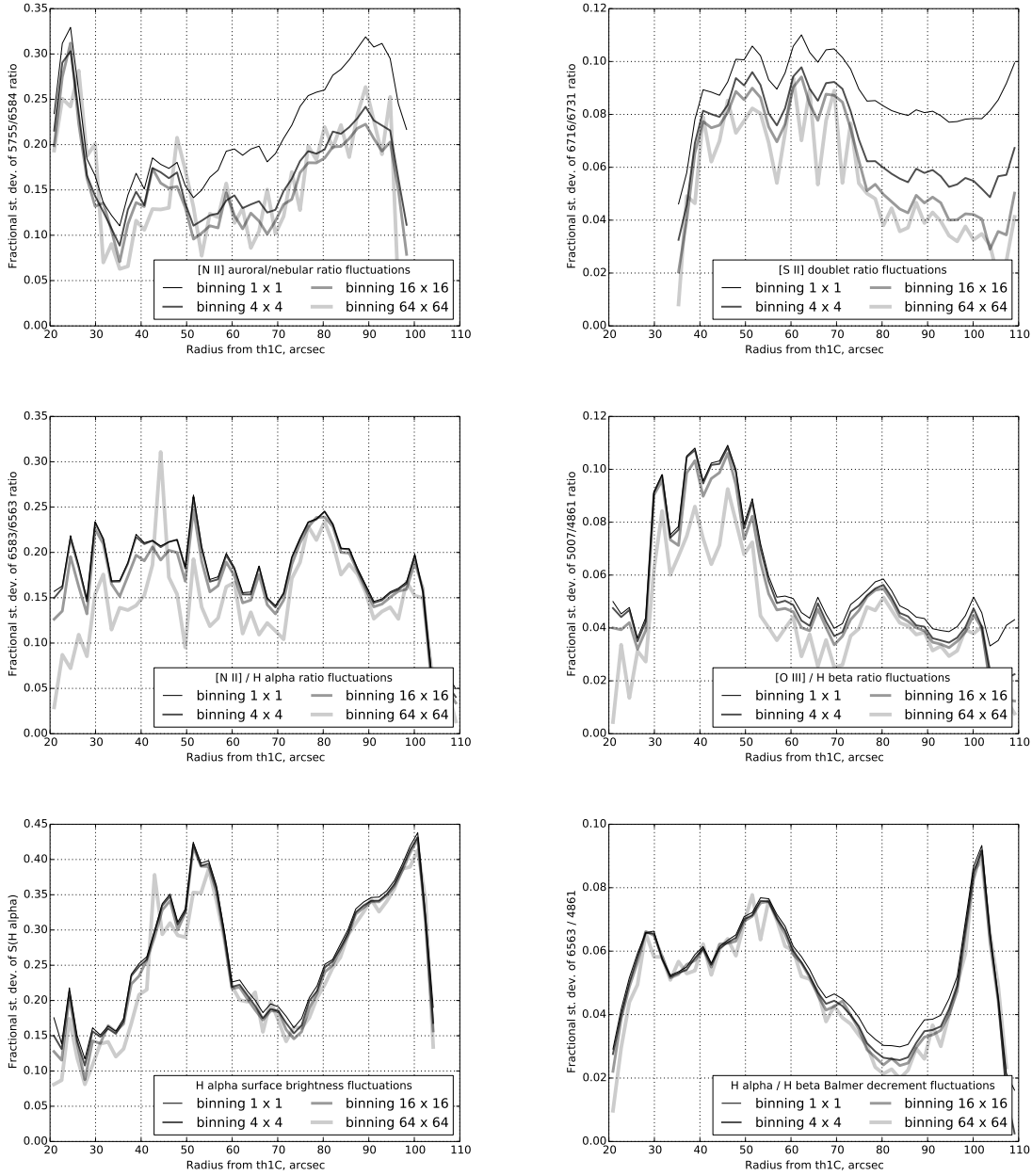


Fig. 8.— Fractional standard deviation of line ratio and surface brightness fluctuations as a function of radius and for different binnings.

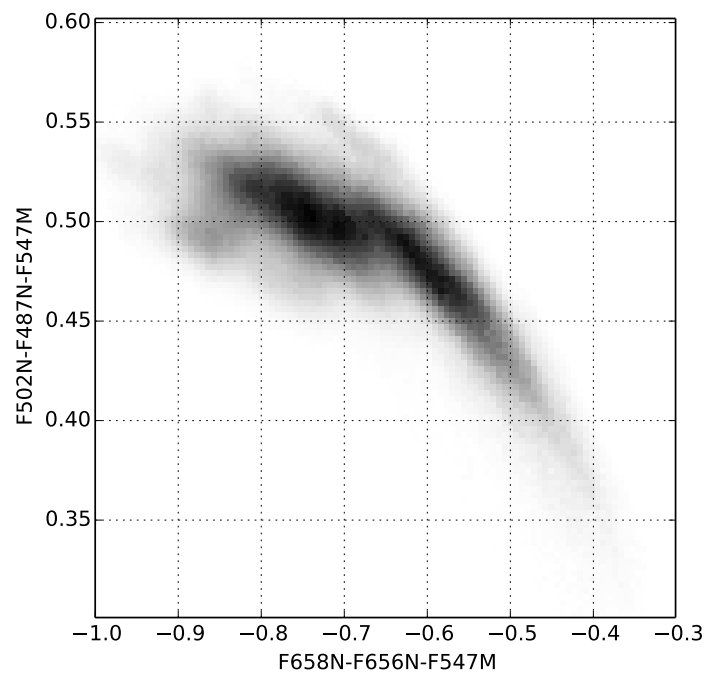


Fig. 9.— Joint distribution of strong line ratios:  $[\text{O III}]/\text{H}\beta$  versus  $[\text{N II}]/\text{H}\alpha$ . The weighting is by the  $\text{H}\alpha$  surface brightness.

## 1.2. Deriving $T_e$ , $n_e$ from line ratios

Figure 10 compares our line ratios with selected measurements from the literature and with the predictions of one-zone emission models with a unique temperature and density. Agreement with previous measurements is good in the bright regions (left of the diagram), but we deviate from Mesa-Delgado for the fainter regions. Part of the increase in 5755/6583 to the left of the diagram is due to higher densities, but there is evidence for an additional temperature increase over and above that.

However, as can be seen from Figure 11, a model with two different density components along the line of sight can also explain the top-left of the diagram. The particular model shown has two components of equal temperature (10,000 K), each with the same emission measure:  $\int n_e n(N^+) dz$ . Over a wide range of parameter space, the [S II] ratio is only sensitive to the density of the lower-density component, while the [N II] ratio is only sensitive to the density of the higher-density component. A density contrast of a factor of 20 ( $10^4 \text{ cm}^{-3}$  and  $2 \times 10^5 \text{ cm}^{-3}$ ) is sufficient to mimic a temperature increase of 3000 K. If this compression were due to a radiative shock, then it would need a Mach number of  $\sqrt{20} \approx 4.5$ , corresponding to a velocity of  $50 \text{ km s}^{-1}$ , which is typical of the jets observed in Orion.

Although the bi-density mechanism can explain small knots and filaments with elevated 5755/6583, it cannot readily explain the general increase in the ratio over a  $10'' \times 10''$  area, as we see in Orion S. A real increase in temperature seems a more likely explanation.

## 1.3. Strong auroral [N II] associated with jet filaments

See Figures 12 to 17. I will also do another figure that zooms in on the optical outflow source region.

Most of the regions with high 5755/6584 ratio are associated with the bases of stellar outflows.

Estimate density in HH529 jet from the H $\alpha$  brightness and observed width. Compare this with the density required in order to explain the 5755/6583 ratio without invoking higher temperature (see Fig. 11).

## 1.4. Analysis of fluctuations in $T_e$ , $n_e$

See Figures 18 and 19, which I need to redo. Also need to consider density fluctuations. Provisional conclusion is that the main contribution to true temperature fluctuations is on rather large scales: 100 linear pixels or larger ( $> 4''$ ,  $> 2000 \text{ AU}$ ). The fluctuations at these scales are modest:  $t^2 = 0.005\text{--}0.010$ . For the bright inner regions, there is power in smaller scales, but their global contribution is small ( $t^2 < 0.003$ ) because only a small fraction of the nebula has small-scale fluctuations, and they may be mainly due to density fluctuations instead. For the faint outer regions, there are essentially zero fluctuations on scales of  $0.4''\text{--}4.0''$ , while the data for scales  $< 0.4''$  are dominated by noise.

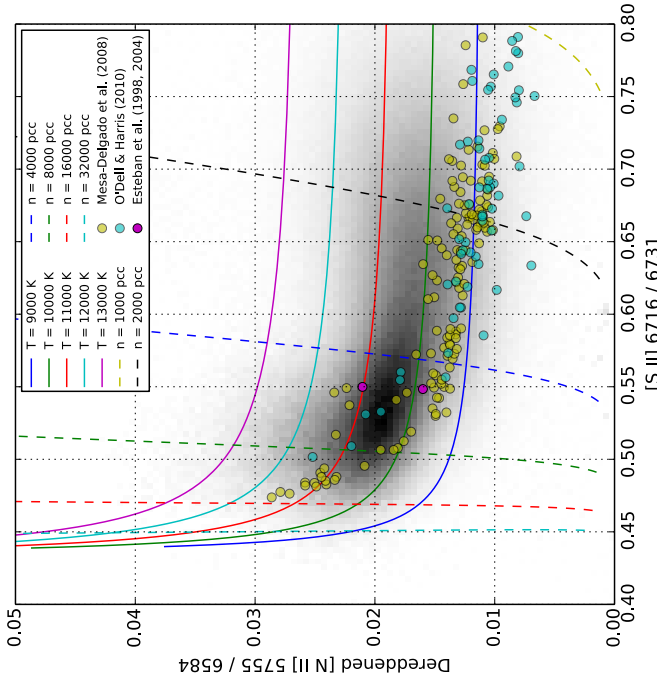


Fig. 10.— Reddening corrected line ratios for [S II] and [N II]

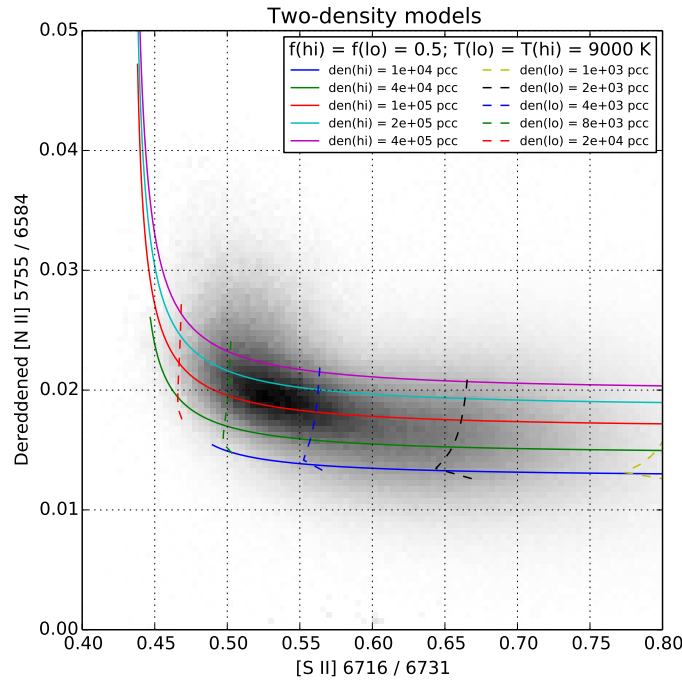


Fig. 11.— Same as Fig. 10 but comparing the observed ratios with constant-temperature, bi-density models.

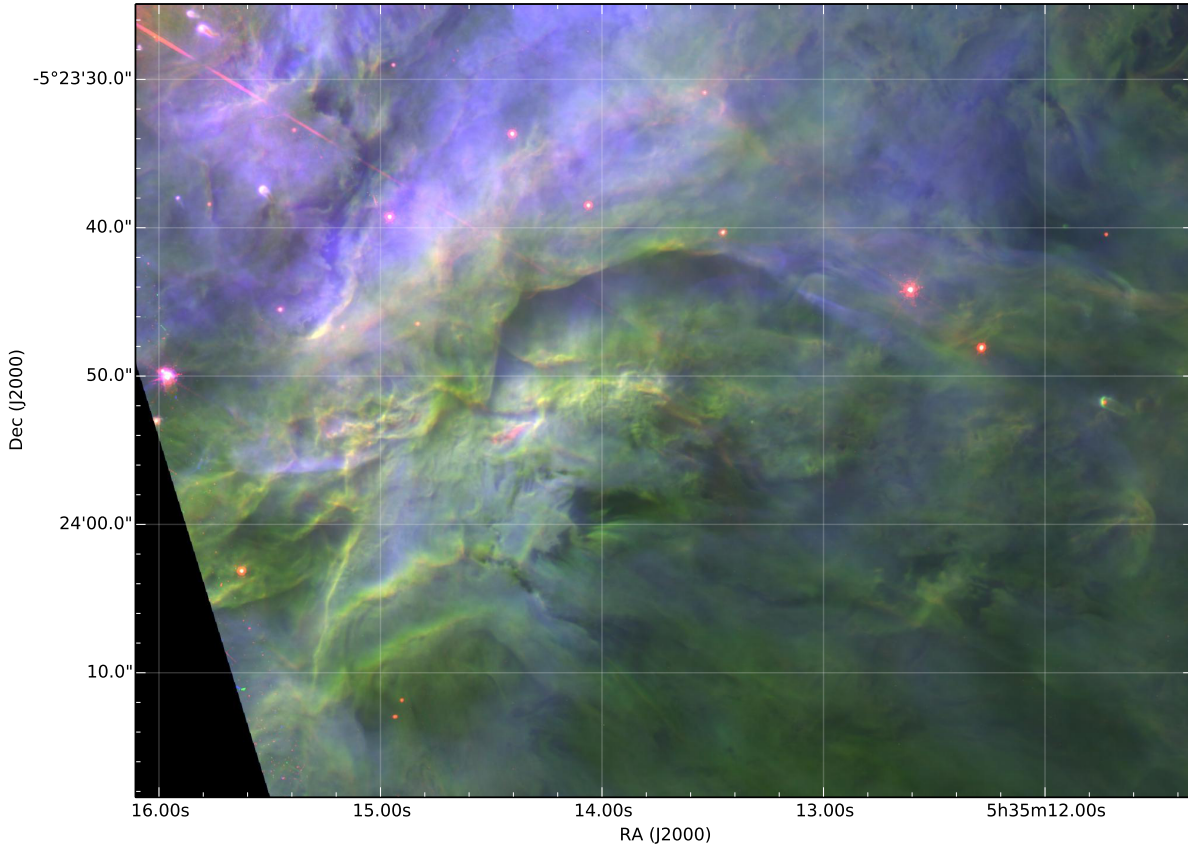


Fig. 12.— Three-color WFC3 image of Orion S region, immediately to the south west of the Trapezium stars, in the light of [S II] 6716+31 (F673N; red), [N II] 6583 (F658N; green) and [O III] 5007 (F502N; blue). The region shown has a size of  $1.2 \times 0.9$  arcminutes. The filters have not been continuum-subtracted, and the F673N filter is the most affected by continuum contamination, so all stars show as red, irrespective of their true colors.

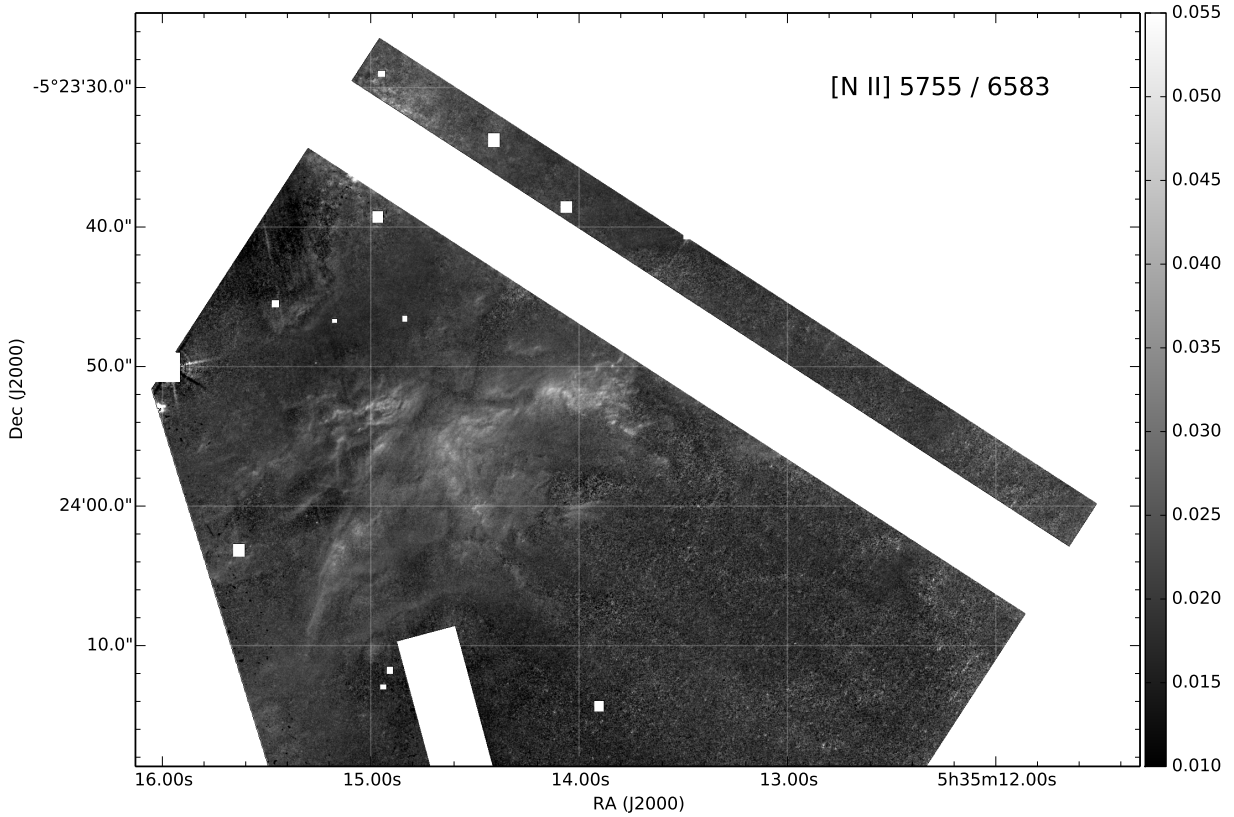


Fig. 13.— Positive grayscale image of the diagnostic [N II] 5755/6583 ratio for the same Orion S region as shown in Fig. 12. Lighter shades imply higher temperatures and/or densities. The positions of bright stars are masked out in the image, as are regions that are badly affected by scattered light from the Trapezium stars, which are just outside the field of view. The ratio is corrected for reddening and calculated according to the procedure outlined in § 1.1.

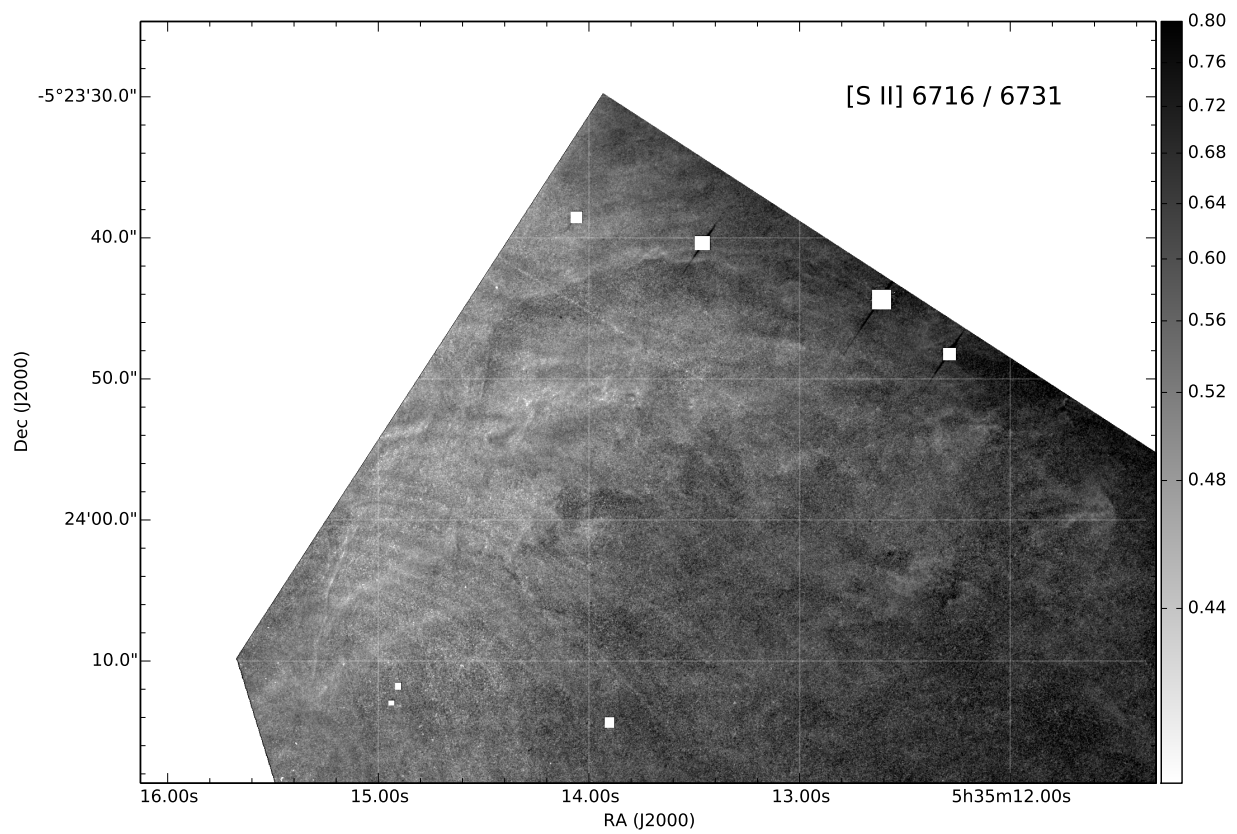


Fig. 14.— Negative grayscale image of the diagnostic [S II] 6716/6731 ratio for the same Orion S region as shown in Fig. 12. Lighter shades imply higher densities.

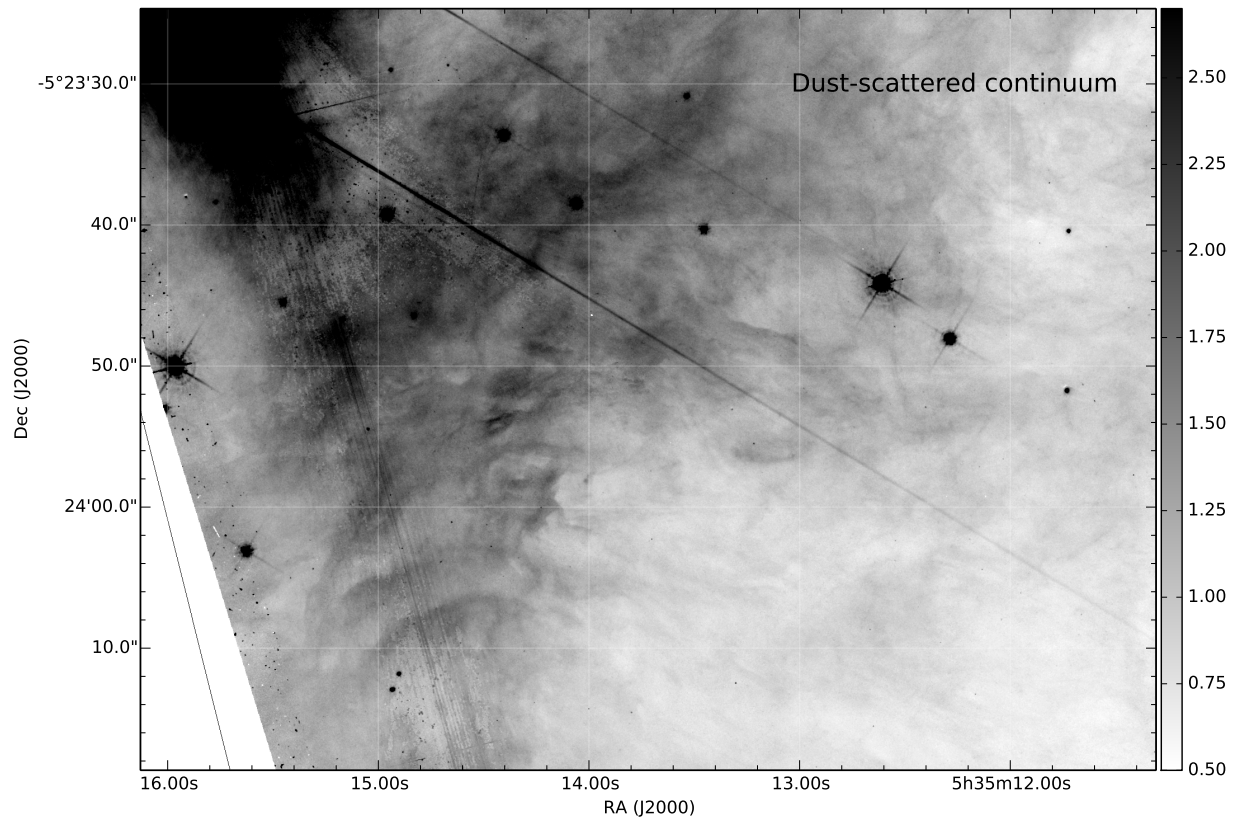


Fig. 15.— Negative grayscale image of dust-scattered continuum for the same Orion S region as shown in Fig. 12. The image was calculated by subtracting an estimate of the atomic recombination continuum from the signal in the F547M filter (see text for details). Darker shades correspond to higher surface brightness.

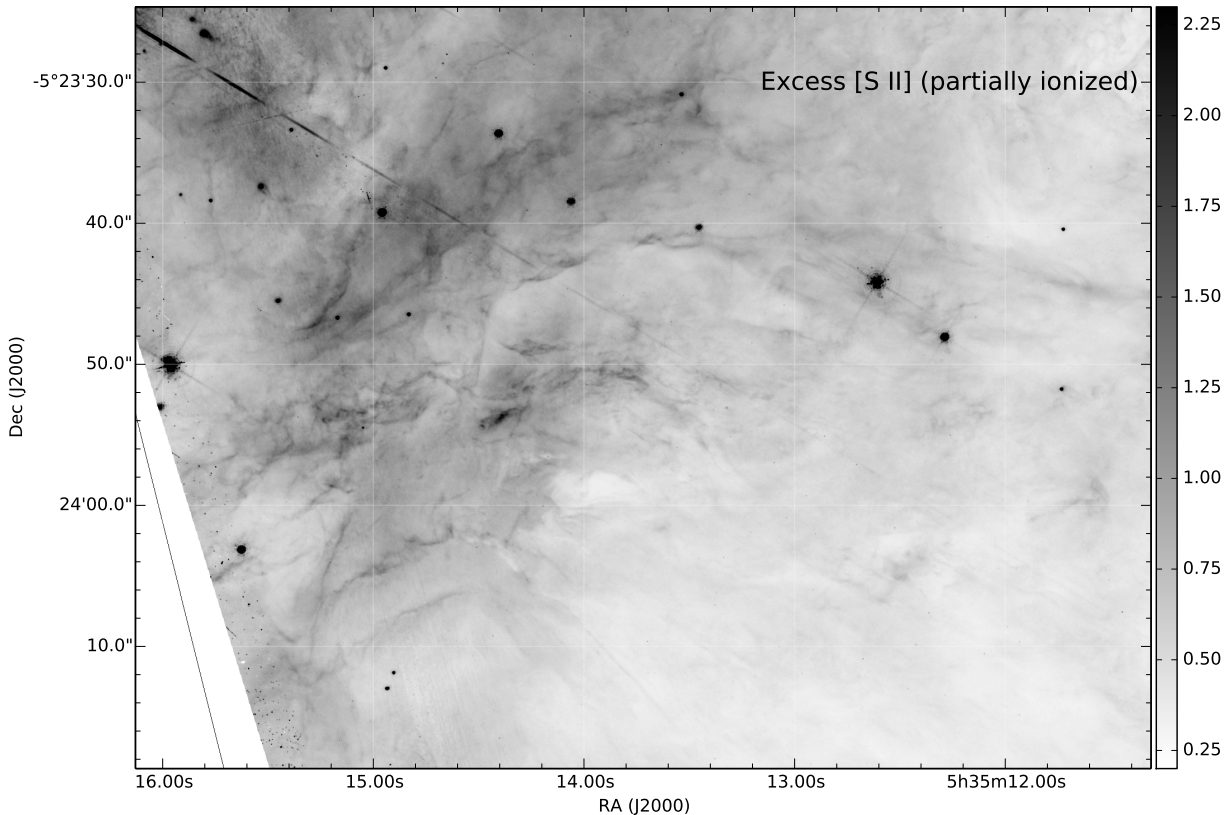


Fig. 16.— Negative grayscale image of “excess” [S II] emission for the same Orion S region as shown in Fig. 12. The image was calculated by subtracting a scaled version of the F658N image from the F673N image. This largely cancels out the portion of the [S II] emission that comes from fully ionized gas, leaving only the emission from partially ionized gas. The resulting thin filaments trace the positions of ionization fronts and low-velocity shocks. Darker shades correspond to higher surface brightness.

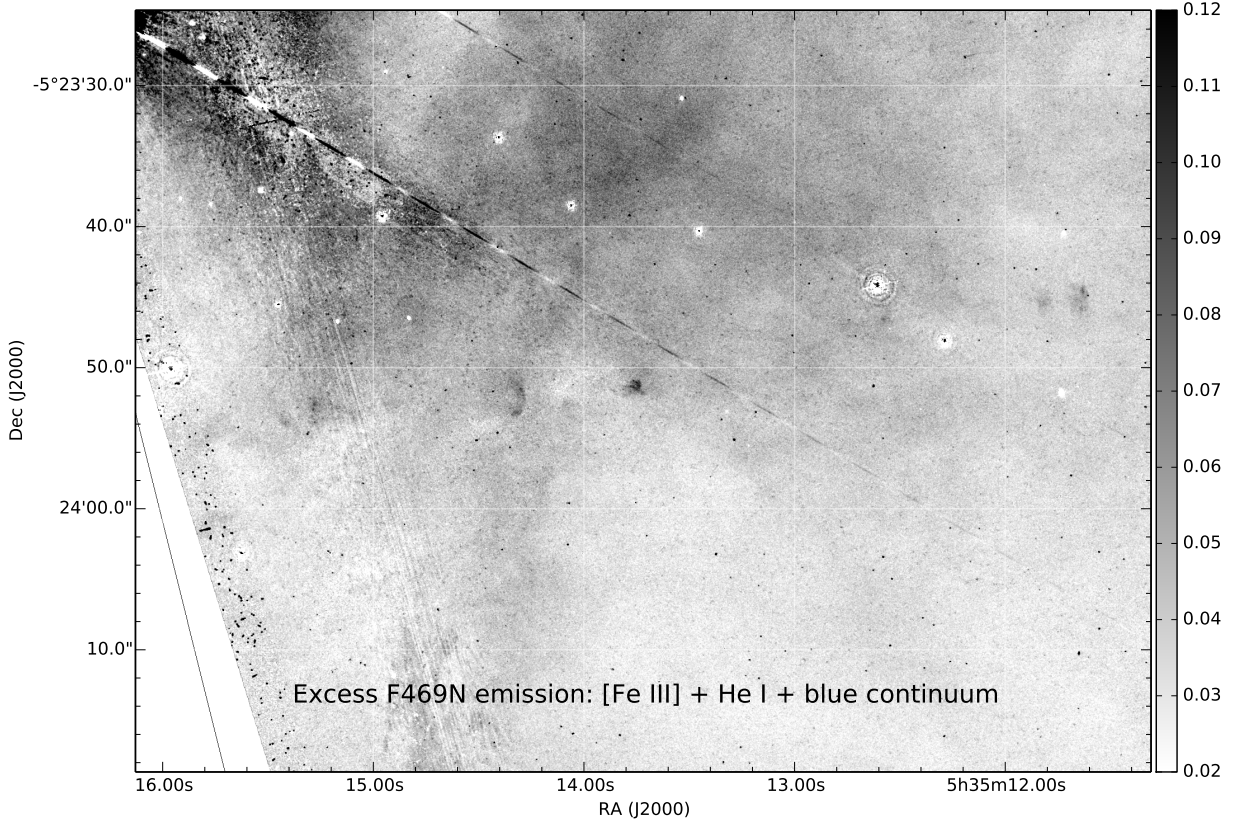


Fig. 17.— Negative grayscale image of “excess” emission in the F469N filter for the same Orion S region as shown in Fig. 12. The image was calculated by subtracting a scaled version of the F547M continuum image from the F469N image. The scaling factor was chosen so as to exactly cancel out the continuum contribution to F469N filter for the average spectrum of the nebula. The residual emission is either bluer-than-average continuum or due to weak emission lines that fall in the filter bandpass (the filter’s ostensible target line, He II 4686, is not observed in the Orion Nebula). The line contribution is likely to be due to [Fe III] 4667+4702, which are extremely weak in usual circumstances, but may be considerably enhanced when silicate dust grains are destroyed in  $\sim 100 \text{ km s}^{-1}$  shocks.

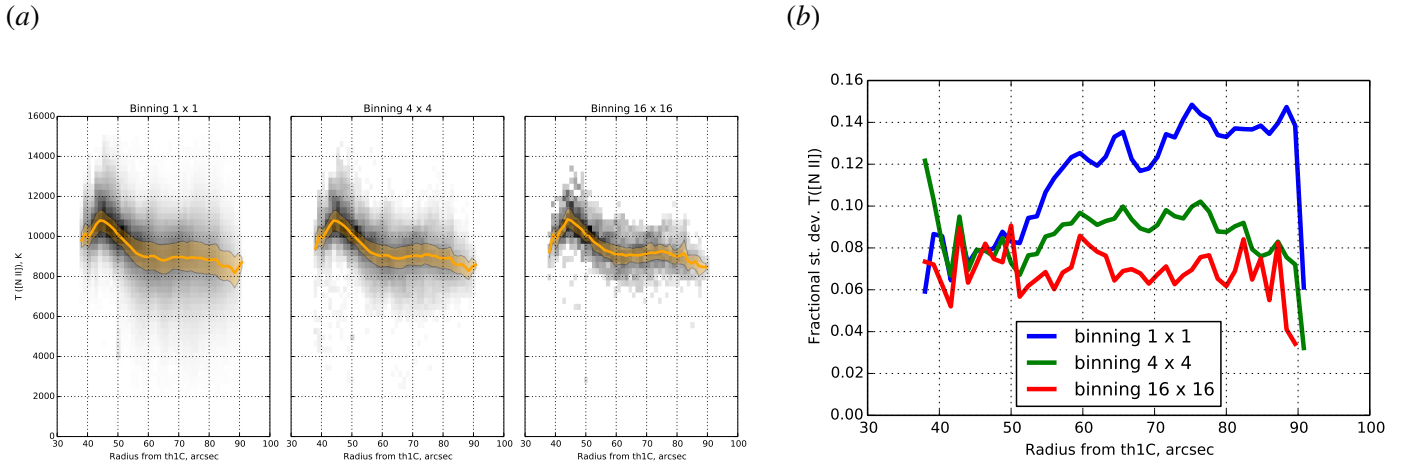


Fig. 18.— This still has an old version of the figure. I need to redo it with the new ratios, but the results will likely not change. (a) Temperature distribution as a function of radius for different binnings. (b) Standard deviation of temperatures as a function of radius for different binnings.

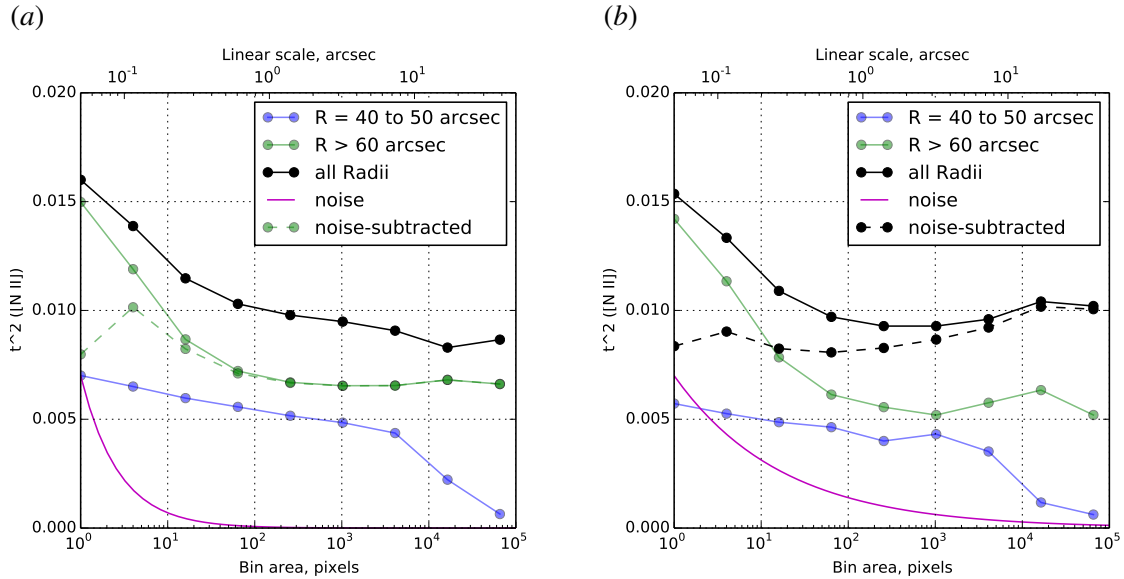


Fig. 19.— This still has an old version of the figure. I need to redo it with the new ratios, but the results will likely not change. Scale-dependence of temperature fluctuations:  $t^2$  as a function of binning. (a) Variance of  $T_e/\bar{T}_e$  for the entire image (black line) and two subsamples: an annulus centered on the high-temperature region (blue line) and the more distant, fainter regions (green line). The magenta line is an estimate of the noise contribution to the full sample, and the dashed black line is the result of subtracting the noise from the observed values. (b) Same as a but using a “robust” estimator of the variance, based on the interquartile range.

## REFERENCES

- Brown, T. M. 2006, Filter Throughputs for WFC3 SYNPHOT Support, Instrument Science Report WFC3 2006-3, Space Telescope Science Institute, Baltimore
- Henney, W. J., O'Dell, C. R., Ferland, G. J., & Peimbert, M. 2014, In prep
- Kalirai, J. S., Baggett, S., Borders, T., & Rajan, A. 2010, The Photometric Performance of WFC3/UVIS: Temporal Stability Through Year 1, Instrument Science Report WFC3 2010-14, Space Telescope Science Institute, Baltimore
- Kalirai, J. S., et al. 2009, WFC3 SMOV Proposal 11450: The Photometric Performance and Calibration of WFC3/UVIS, Instrument Science Report WFC3 2009-31, Space Telescope Science Institute, Baltimore
- Mesa-Delgado, A., Esteban, C., & García-Rojas, J. 2008a, ApJ, 675, 389
- . 2008b, ApJ, 675, 389
- Núñez-Díaz, M. 2013, PhD thesis, Departamento de Astrofísica, Universidad de La Laguna
- O'Dell, C. R., Ferland, G. J., Henney, W. J., & Peimbert, M. 2013, AJ, 145, 92
- O'Dell, C. R., & Harris, J. A. 2010, AJ, 140, 985
- Sabbi, E., & the WFC3 Team. 2013, WFC3 Cycle 20 Calibration Program, Instrument Science Report WFC3 2013-05, Space Telescope Science Institute, Baltimore

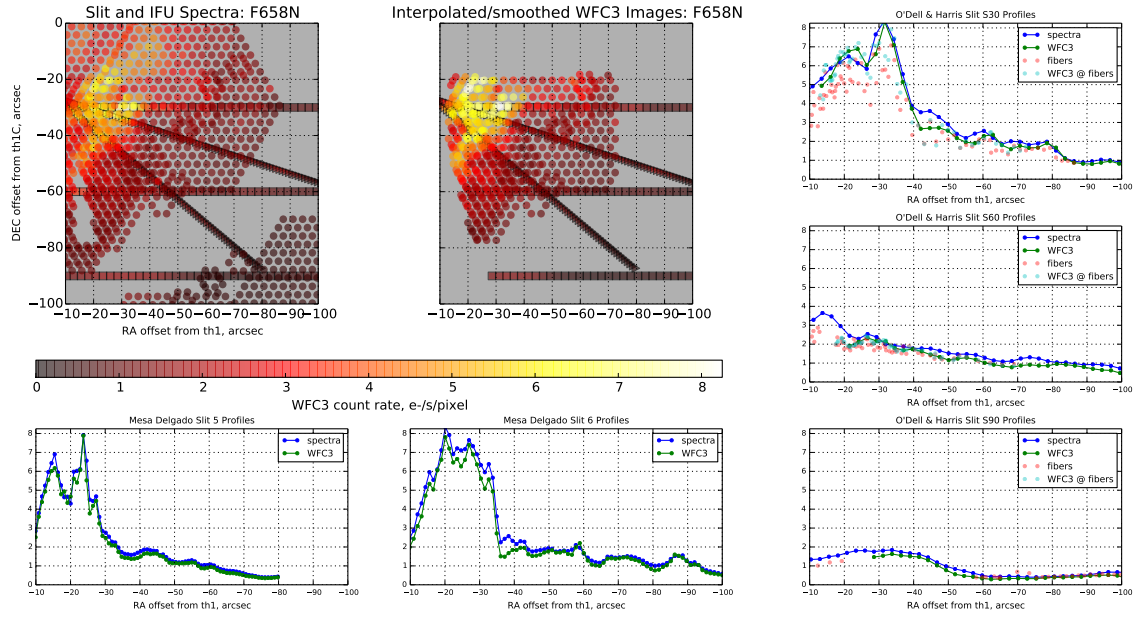


Fig. 20.— Example of the procedure for calibrating a WFC3 filter using longslit and IFU spectrophotometry of the Orion Nebula. The upper-left panel shows a map of the surface brightness in the F658N filter derived from integral field unit observations (circles; Núñez-Díaz 2013) and longslit observations (squares; O’Dell & Harris 2010 and triangles; Mesa-Delgado et al. 2008b). In each case, the observed spectrum was folded through the nominal filter transmission profile to obtain a predicted WFC3 count rate. The upper-center panel is the same, but for the actual WFC3 observations in the F658N filter, after smoothing the WFC3 images to the respective ground-based resolutions and integrating over a synthetic aperture corresponding to each spectrophotometric sample.

### A. Calibration of the WFC3 filters

In a recent study (O’Dell et al. 2013) of NGC 6720, the Ring Nebula, evidence was found for significant deviations of some WFC3 UVIS narrow-band filter calibration constants from the pre-launch determined values given in the WFC3 Instrument Handbook. Several observationally important diagnostic line ratios are significantly impacted by the filter calibrations in question. It is therefore of paramount importance to confirm the calibrations under a wider range of nebular excitation conditions. The Orion Nebula, M42, provides an excellent complement to NGC 6720 in this respect, since it is of lower ionization and temperature, allowing the calibration to be extended to smaller values of the emission line equivalent widths, where continuum contamination of the narrow band filters is greater. At the same time, extensive high-quality spectrophotometric data exists for this object, obtained by distinct teams, using multiple telescopes and instruments (for example, Mesa-Delgado et al. 2008a; O’Dell & Harris 2010). This allows the true spectrum to be determined with a degree of precision and confidence that is impossible for other objects.

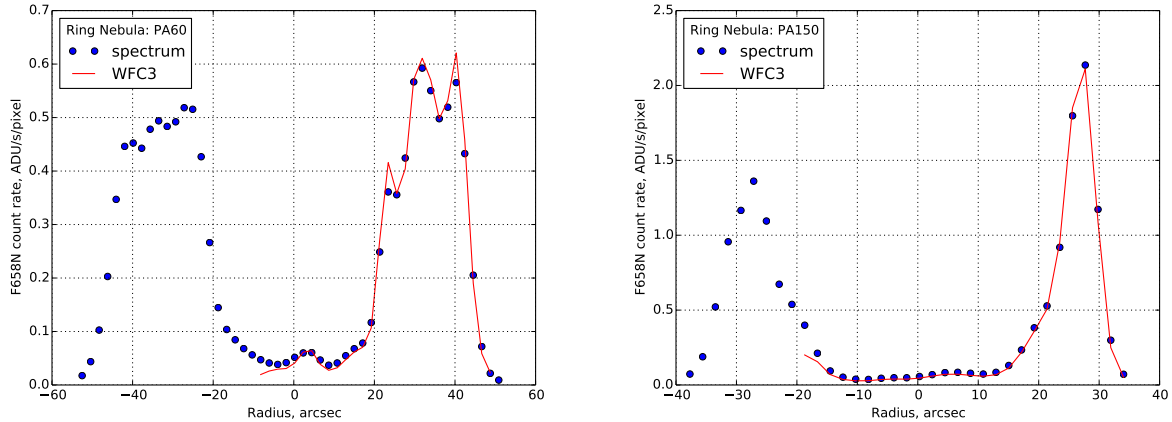


Fig. 21.— Example of the procedure for spectrophotometrically calibrating a WFC3 filter.

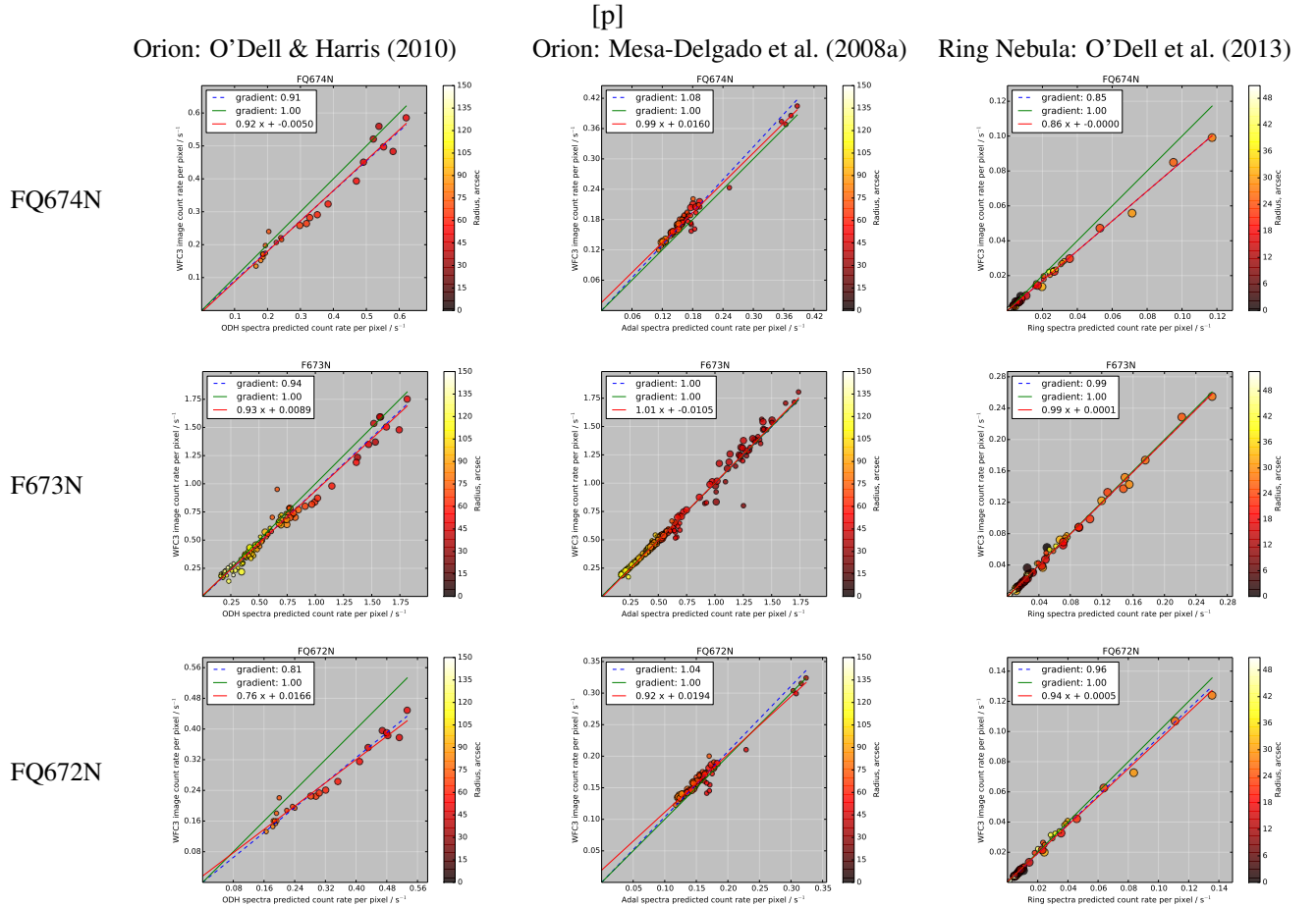


Fig. 22.— Results of spectrophotometric calibration of the nebular [S II] filters of WFC3. On the vertical axis is plotted the observed filter count rate in a series of synthetic apertures that coincide with spectrophotometric observations. On the horizontal axis is plotted the predicted count rate calculated by folding the observed spectrum through the nominal filter transmission profile. The solid line shows a slope of unity, which is what would be expected if the nominal throughput were correct. The dashed line shows the best-fit slope.

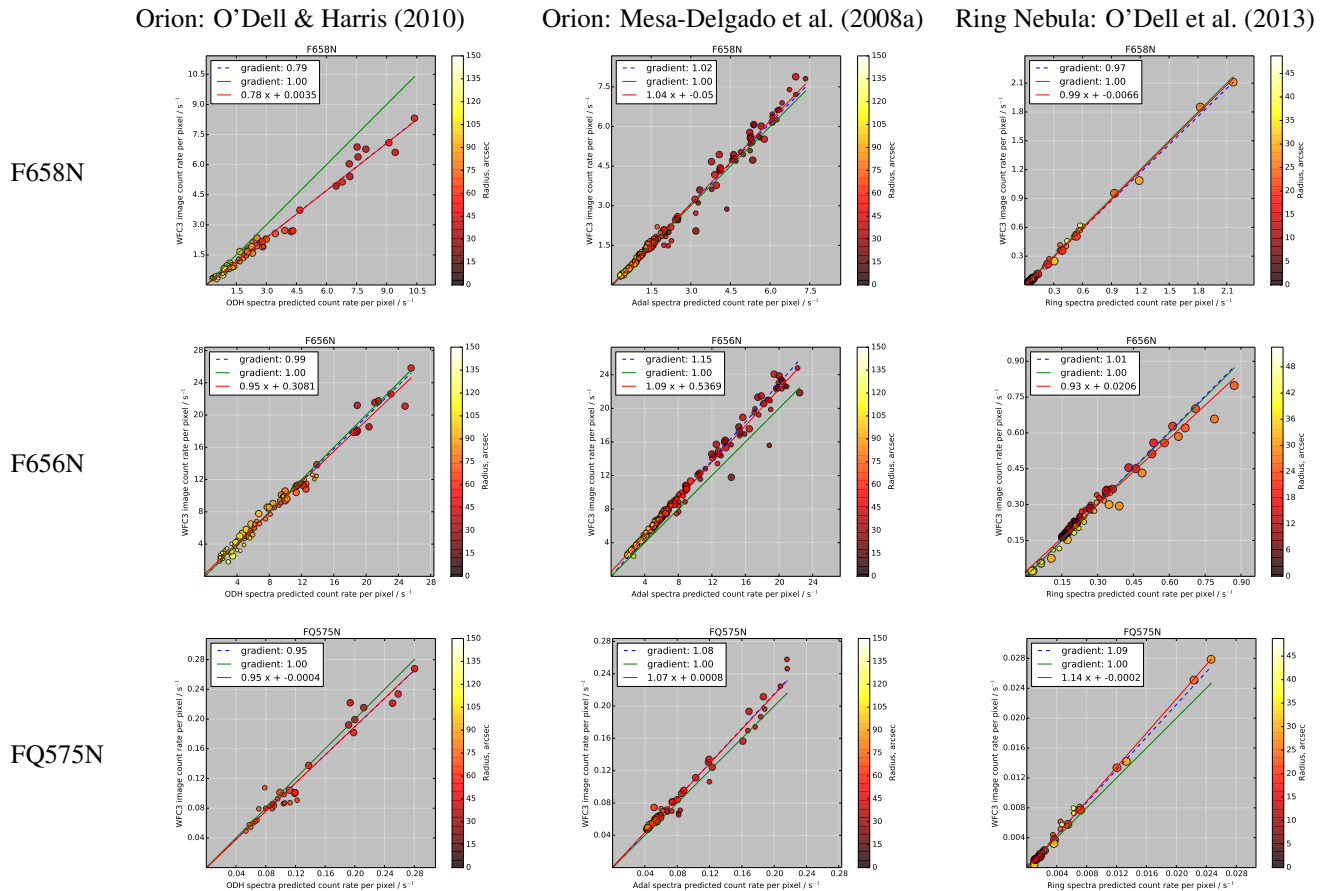


Fig. 23.— Same as Fig. 22 but for the nebular [N II], H $\alpha$ , and auroral [N II] filters.

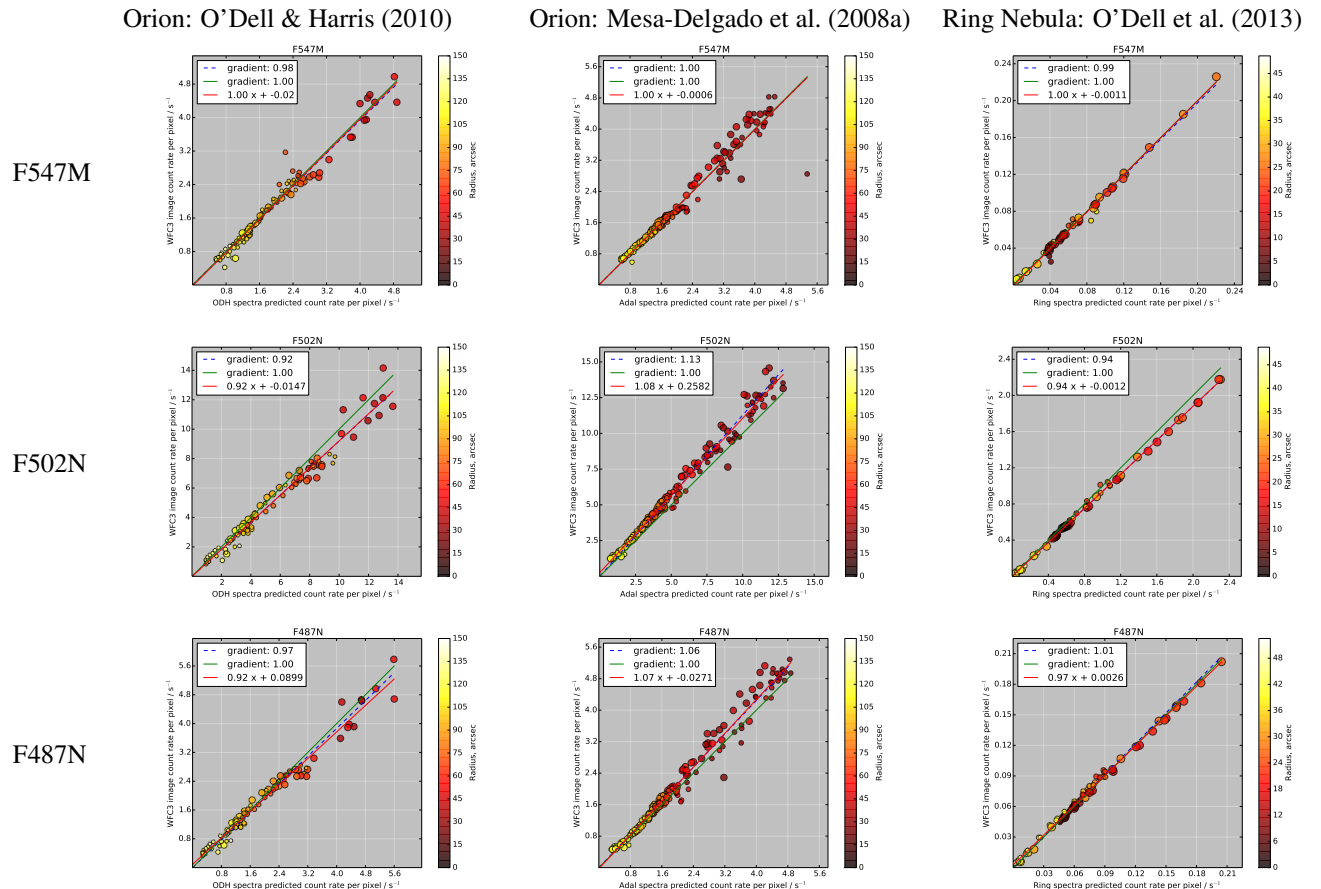


Fig. 24.— Same as Fig. 22 but for the green medium-band continuum, nebular [O III], and H $\beta$  filters.

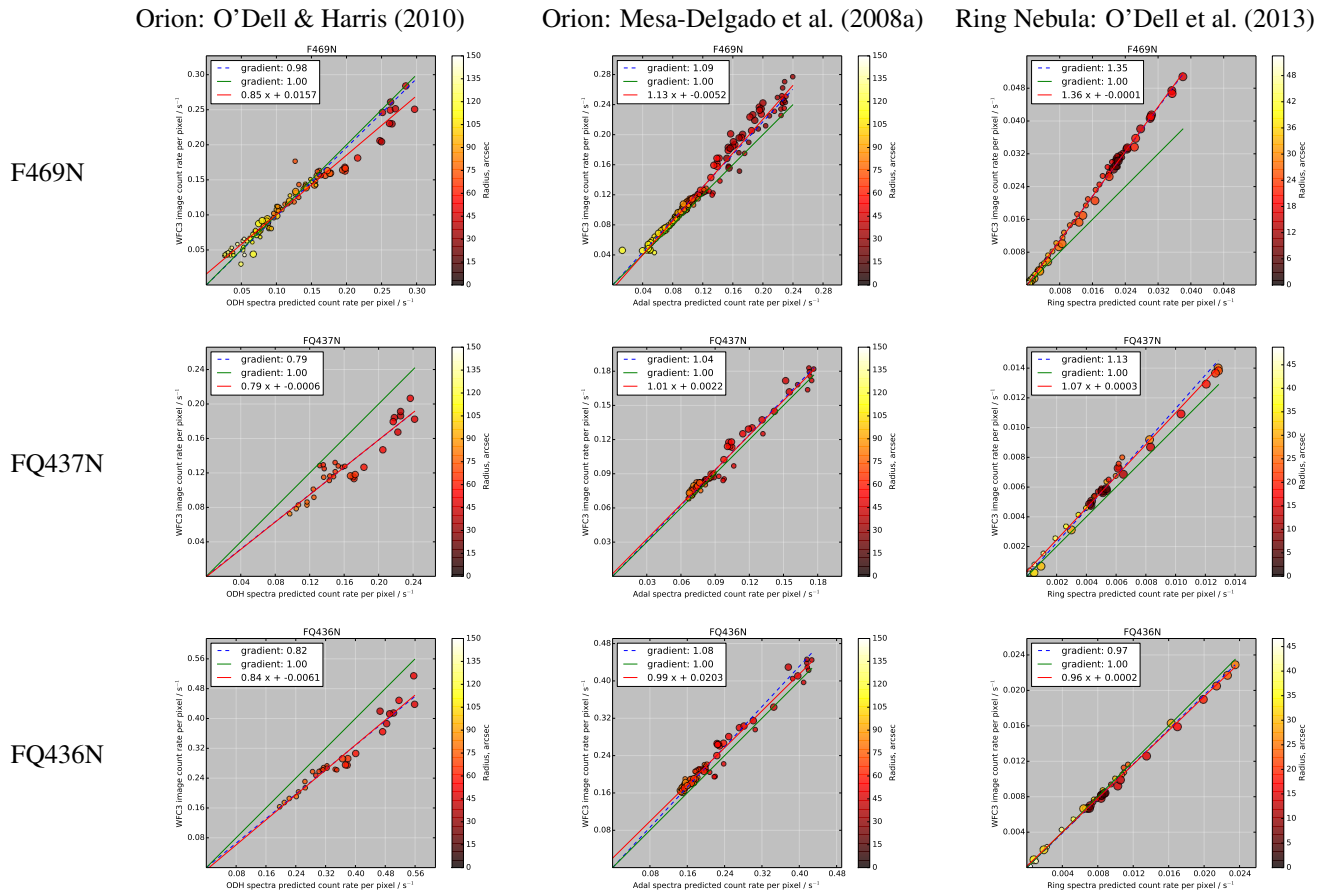


Fig. 25.— Same as Fig. 22 but for the [He II] and auroral [O III] filters.